

## Using ARTEMIS pickup ion observations to place constraints on the lunar atmosphere

J. S. Halekas,<sup>1,2</sup> A. R. Poppe,<sup>1,2</sup> G. T. Delory,<sup>1,2</sup> M. Sarantos,<sup>2,3,4</sup> and J. P. McFadden<sup>1</sup>

Received 29 October 2012; revised 19 November 2012; accepted 24 November 2012.

[1] We present a method for deriving constraints on the structure and composition of the lunar atmosphere by using pickup ion measurements from ARTEMIS, mapping observed fluxes from the spacecraft location to derive production rates at the source region, and fitting to a parameterized neutral atmosphere model. We apply this technique to ~12 min of high-resolution burst data collected by ARTEMIS P2 above the sunlit lunar surface, in the dawnside terrestrial magnetosheath. During this time period, ARTEMIS observed multiple velocity components, requiring the presence of multiple species and/or source regions. We use species at or near masses 12, 16, 24, 28, and 40 to derive a best-fit model that proves consistent with most known abundances and limits on neutral densities as well as predictions thereof. However, we find indications of large neutral abundances at mass ~16, exceeding optical limits on oxygen by a factor of ~20, possibly indicating either “seeding” of the Moon by terrestrial oxygen during its magnetotail passage or significant contributions by OH or CH<sub>4</sub>. We also derive new upper limits on the abundance of OH and Al in the atmosphere.

**Citation:** Halekas, J. S., A. R. Poppe, G. T. Delory, M. Sarantos, and J. P. McFadden (2013), Using ARTEMIS pickup ion observations to place constraints on the lunar atmosphere, *J. Geophys. Res.*, 118, doi:10.1029/2012JE004292.

### 1. Introduction

[2] More than 40 years after the Apollo program, the lunar atmosphere remains poorly known. We have measured only a few of the neutral species in the atmosphere, including the alkali atoms Na and K and the noble gases He and Ar [Potter and Morgan, 1988; Hoffman *et al.*, 1973; Stern, 1999; Stern *et al.*, 2012], some unconfirmed hints of nitrogen- and carbon-based molecules [Hoffman and Hodges, 1975], and only upper limits from spectroscopy on others (e.g., Feldman and Morrison [1991]). The list of measured species lengthens slightly if we include ionized products, with evidence for O<sup>+</sup>, Al<sup>+</sup>, and C<sup>+</sup> [Mall *et al.*, 1998; Yokota *et al.*, 2009] (although some of these could instead represent sputtering products). Regardless, a gap remains between the list of species that should exist [Stern, 1999; Sarantos *et al.*, 2012a] and those we have measured. Next year, the Lunar Atmosphere and Dust Environment Explorer (LADEE) mission should fill in many

of these unknowns using both in situ spectrometry and remote spectroscopy. However, with ARTEMIS [Angelopoulos, 2010], a two-probe mission currently in highly elliptical lunar orbits, we have an opportunity now to lay the groundwork for LADEE.

[3] The two ARTEMIS probes carry ion sensors (ESA) [McFadden *et al.*, 2008] that can measure ionized lunar products albeit without composition information. A variety of mechanisms, including direct sputtering from the surface, and ionization (primarily photoionization) of neutral atmospheric species, can act to produce ions in the lunar environment. The neutrals themselves derive from a host of processes, including thermal and chemical processes at the surface, sputtering, photostimulated desorption, and micro-meteorite impact, some of which vary significantly during the Moon’s orbit around the Earth. Once ionized, atmospheric constituents feel the effects of magnetic and electric fields in the ambient plasma and follow cycloidal “pickup” trajectories with a characteristic scale proportional to their mass.

[4] By measuring the fluxes of pickup ions from lunar orbit and tracing their trajectories back to their source location, we can learn about the lunar atmosphere and the processes that control it. Previously, Halekas *et al.* [2012] published a sample of 29 pickup ion events observed by ARTEMIS in the solar wind, most at distances of 5000–10,000 km from the Moon, and analyzed their trajectories to place constraints on the major constituents. That paper found that the dominant constituent for most solar wind events seen by ARTEMIS lies in the mass range ~20–40. However, given the small number of observations (most with relatively few spectra) and an analysis that only considered the peak of the pickup ion flux, this previous

<sup>1</sup>Space Sciences Laboratory, University of California, Berkeley, California, USA.

<sup>2</sup>NASA Lunar Science Institute, NASA Ames Research Center, Moffett Field, California, USA.

<sup>3</sup>Heliophysics Science Division, NASA Goddard Space Flight Center, Greenbelt, Maryland, USA.

<sup>4</sup>Goddard Planetary Heliophysics Institute, University of Maryland, Baltimore, Maryland, USA.

Corresponding author: J. S. Halekas, Space Sciences Laboratory, University of California, 7 Gauss Way, Berkeley, CA, USA. (jazzman@ssl.berkeley.edu)

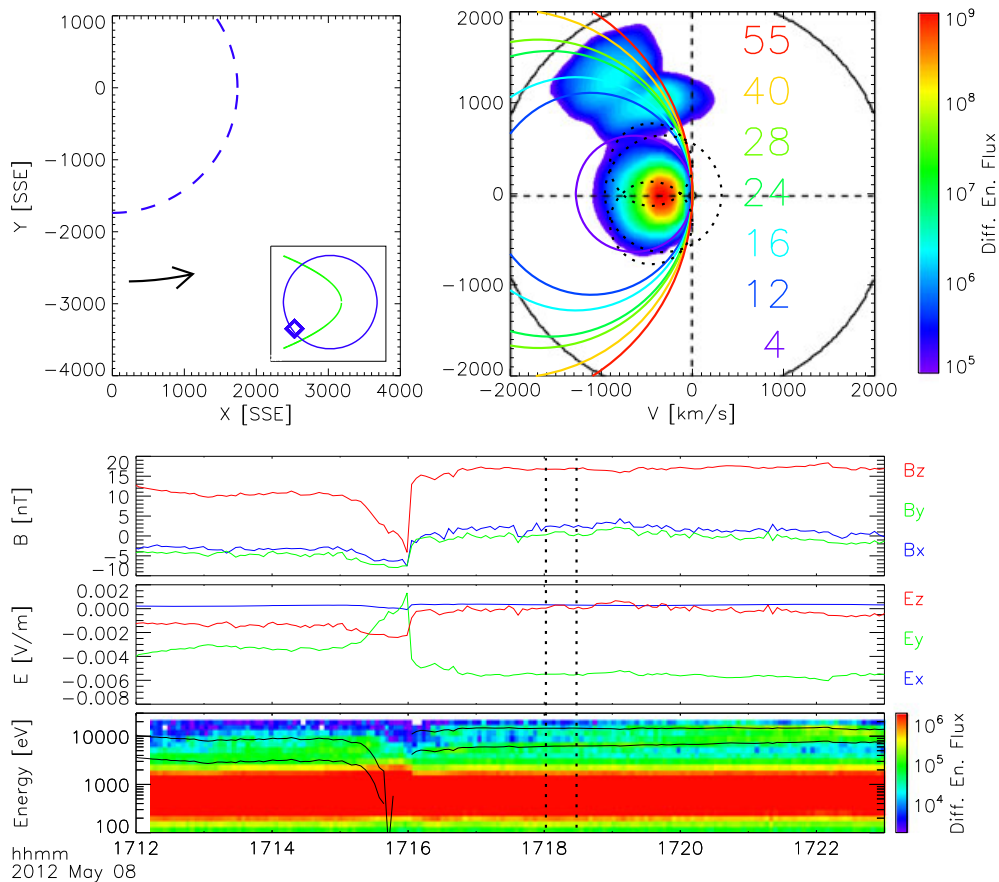


**Figure 1.** Overview of a pickup ion event observed by ARTEMIS P2 in the terrestrial magnetosheath, showing (top left) spacecraft trajectory (with an inset showing position in lunar orbit and average bow shock position), (top right) sample ion velocity distribution in plane perpendicular to the magnetic field, and (bottom) time series of magnetic field, derived electric field, and angle-averaged differential energy flux [ $\text{eV}/(\text{eV cm}^2 \text{ s sr})$ ]. Note different flux scale appropriate for angle-averaged data (bottom). Colored circles on velocity distribution show expected velocities for various pickup ion species; dashed black circles show velocities for protons reflecting at a selection of angles. Dashed lines on time series plot indicate time range of sample velocity distribution; solid lines (bottom) show expected energies for pickup ions originating from directly below the spacecraft (lower line) and from the subsolar point (upper line).

work could place few constraints on the mix of species and did not attempt to relate ion fluxes to source densities.

[5] Theoretical tools now exist, which allow us to relate observed ion fluxes to source rates in the atmosphere, given knowledge of the ion mass and trajectory [Hartle *et al.*, 2011; Sarantos *et al.*, 2012b]. With sufficient constraints, one can use pickup ion data to constrain the composition and structure of the lunar atmosphere. In this paper, we consider an ARTEMIS observation of an event in the dawnside terrestrial magnetosheath for which we have high-resolution burst data, for the first time providing us with enough data points to attempt such a study.

## 2. ARTEMIS Observations

[6] Figure 1 shows an overview of the event considered in this paper. At the time of this observation, the Moon (and ARTEMIS) sat near the edge of the Earth’s magnetosheath, just before the Moon exited into the solar wind. The Moon had resided in the magnetosheath for  $\sim 30$  h at this time, after

traversing the tenuous magnetotail lobes for several days. The P2 probe had just passed the dawn terminator at the start of the interval, with a sunward trajectory close to the ecliptic. The magnetic field had a dominant  $B_z$  component, resulting in the  $-E_y$  electric field component needed to efficiently accelerate pickup ions toward the spacecraft. A large field rotation at 17:16 fortuitously triggered the onboard burst system and provided us with high time and angular resolution throughout this interval. We observe multiple components in the angle-averaged energy spectra, indicating the presence of different species and/or source locations. The velocity distribution in the upper right panel shows that these components have velocities roughly consistent with pickup ions in the mass range 12–55 and inconsistent with reflected protons from the surface or crustal magnetic fields [Saito *et al.*, 2008; Lue *et al.*, 2011].

[7] This time period had very useful characteristics. The relatively large 15–20 nT magnetic field and the low  $\sim 300$  km/s flow velocity ensure a small ratio of ion gyroradius to lunar radius. This correspondingly reduces the relative scale of pickup ion trajectories and allows us to observe

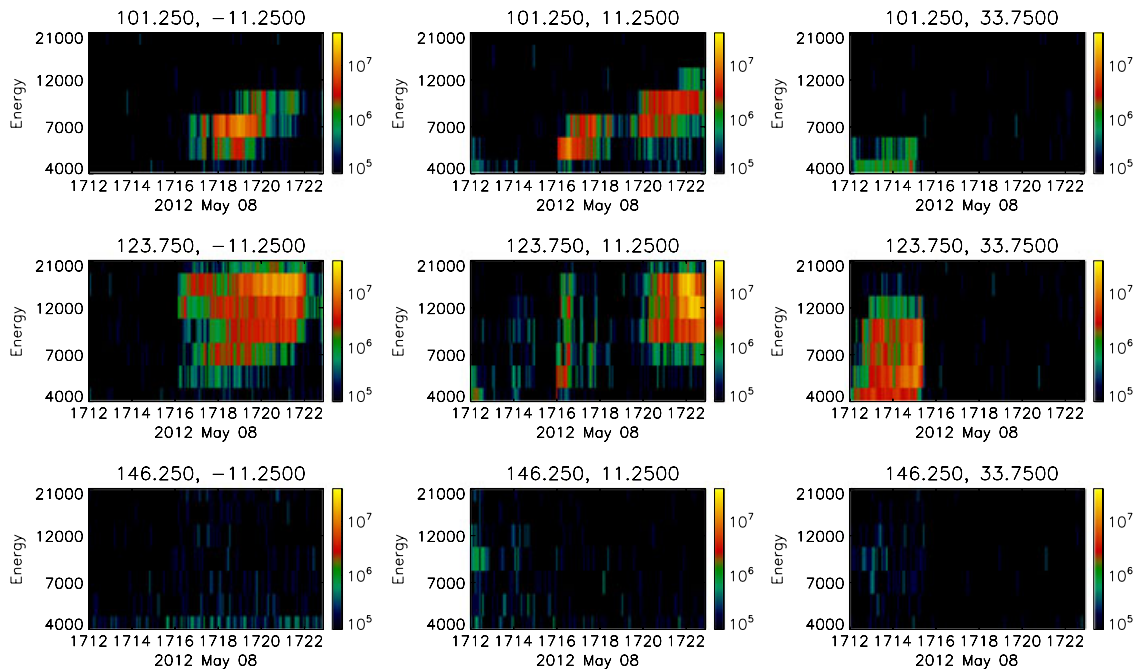


**Figure 2.** Measured pickup ion differential energy fluxes [eV/(eV cm<sup>2</sup> s sr)] in nine ESA angle bins (panel titles indicate spacecraft  $\varphi$  and  $\theta$ ) as a function of energy and time.

multiple ion species with well-separated trajectories relatively near the Moon but still far enough from the surface that reflected protons from the surface and/or crustal magnetic fields that do not obscure the pickup ion signal.

[8] The angle-averaged spectra and velocity distribution shown in Figure 1 help give some idea of the pickup ion characteristics, but to fully reveal the complexity of the event and the constraints that we can put on the source(s), in Figure 2 we display pickup ion fluxes as a function of energy and time for nine different ESA instrumental angle bins. The distribution of flux versus instrument  $\theta$  (the angle from the probe spin plane, which lies close to the ecliptic) primarily relates to geometrical effects, because we can only observe pickup ions where the plane perpendicular to the magnetic field intersects the instrument field of view. However, the distribution of flux versus  $\varphi$  (the angle from the Sun direction, in the spacecraft spin plane), energy, and time relates to the distribution of source locations and species. The energy corresponds to the distance the ion has traveled perpendicular to the plasma flow (along the convection electric field) from its source, whereas the  $\varphi$  angle roughly indicates the degree to which the ion trajectory has bent, which in turn depends on the distance from the source location and the ion mass. The time variability of all of the observations also provides important information because the spacecraft moves  $\sim 1000$  km during the observation period.

[9] We further note that some aspects of the variable pickup ion signature are not at all trivial to understand. In particular, the primary effect leading to the two separate energy components seen in Figure 1 proves somewhat subtle. As shown by Halekas *et al.* [2012], pickup ions that can reach the spacecraft at a given point lie along a curved “line of origins” in the plane intersecting the spacecraft and

perpendicular to the magnetic field. Some portions of that curve lie below the surface of the Moon during our observation period, rendering some energy/mass combinations inaccessible to the spacecraft.

### 3. Constraining Neutral Exosphere Source Models

[10] Hartle *et al.* [2011] have devised a theoretical framework that we use to relate observed pickup ion fluxes to production rates in the exosphere. They found that the vector flux  $n(\vec{v}) = 2r_g \int \bar{v} R(\vec{r}_0) \delta(\bar{v}^2 - 2\bar{v}_x) d^3\bar{v}$ , where  $r_g$  is the ion gyroradius,  $\bar{v} = \vec{v}/V_D$  is the pickup ion velocity normalized by the drift velocity, and  $R(\vec{r}_0)$  is the production rate at the source point corresponding to each trajectory in the integrand. We can conveniently parameterize this equation in terms of the ion gyroangle  $\theta$ , allowing us to use the simple 2-D analytical form [ $X = X_0 + r_g * (\theta - \sin(\theta))$ ,  $Y = Y_0 + r_g * (1 - \cos(\theta))$ ] to trace trajectories for a given ion mass back to their source location (coordinates in the plane perpendicular to  $B$ , aligned with the drift velocity and the electric field). We then take each differential energy flux measurement (converted to units of flux using the known ESA energy and angle response) and calculate a set of partial integrals corresponding to trajectories that contribute to that particular energy-angle bin at that time (using the instantaneous measured ion velocity and magnetic field and the derived convection electric field to analytically back-trace the relevant trajectories). We subdivide the gyroangle into 3600  $0.1^\circ$  subranges and calculate a partial integral for each gyroangle contributing to the given measurement bin for each possible ion species. We thereby arrive at a set of partial integrals

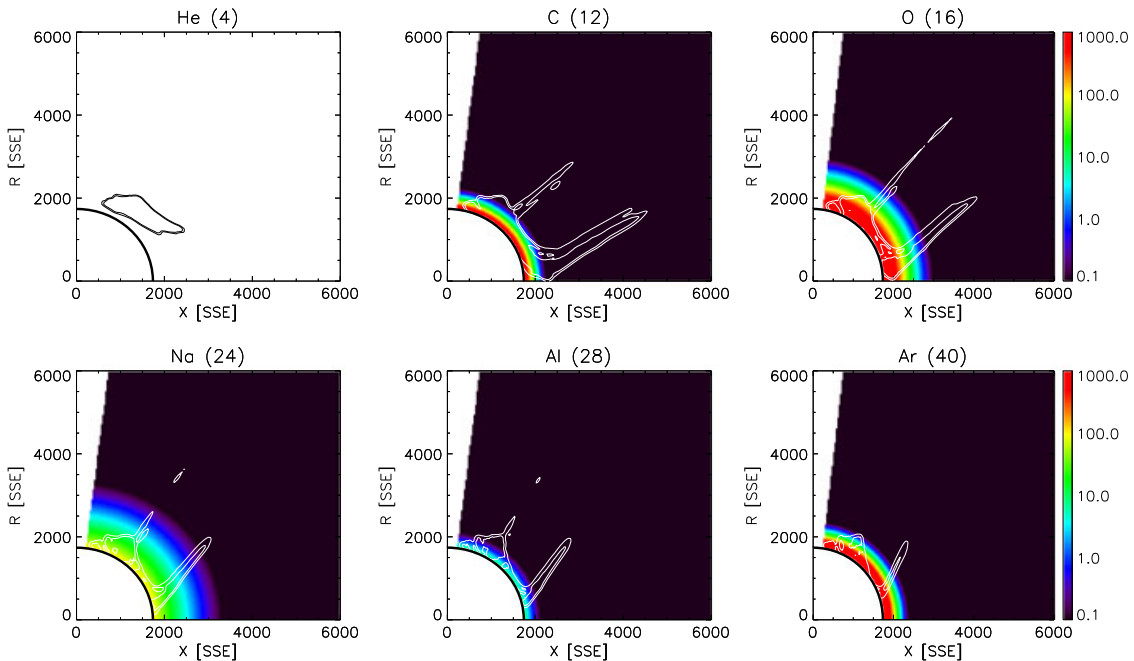


**Figure 3.** Locations of possible sources of pickup ion fluxes measured by ARTEMIS, in cylindrical coordinates, for six different ion masses, with contours indicating total density of source points for all energies, angles, and times during the observation interval. The colored backgrounds of each panel show derived exospheric density distributions corresponding to a best-fit exospheric model, assuming the species indicated produce the major contribution at that ion mass (as described in the text and Table 1). We also show the coverage for He, which we did not use in the final fit.

contributing to each ESA measurement, which in turn map to a set of source points, for each ion mass. We can then weigh these by any assumed form for the exospheric production rate, allowing us to relate an assumed exospheric composition and structure to the fluxes that ARTEMIS would observe.

[11] Naturally, we wish to solve the inverse problem and derive the exospheric composition and structure from the measured fluxes. This problem corresponds to an inversion of a highly overconstrained matrix relating a large number of flux measurements (10,143 data points from 161 times 9 angles  $\times$  7 energies cover the portion of the ESA data containing the observed pickup ion fluxes) to a chosen parameterization of the exosphere. Typically, one solves such a problem by finding the best-fit solution using an appropriate metric. We found that a least-squares metric overemphasized the peak fluxes and under-utilized the constraints provided by the lower fluxes at the shoulders of the distribution. Therefore, we elected to minimize the normalized  $\chi^2$  metric  $\chi^2 = 1/N_X \sum (X_i - Y_i)^2 / (\sigma_{X_i}^2 + \sigma_{Y_i}^2)$ , where  $X_i$  represents a model flux calculated using the prescription above and  $Y_i$  represents the measured flux in that bin. For errors, we assumed  $\sqrt{N}$  counting statistics for both model and measured fluxes. For the model, errors relate to inaccuracies in measured fields and the resulting trajectory reconstruction rather than counting statistics; however,  $\sqrt{N}$  provides a reasonable approximation because errors scale roughly with the magnitude of the fluxes (which scales with count rate). We used a gradient-descent curve-fit algorithm with random initializations to converge to a best fit (or set of best fits) to a model exosphere that best reproduces measured fluxes.

[12] With this machinery in place, we can easily test any chosen parameterization of the exosphere. We experimented with many functional forms and mixes of species and settled on a fit to five ion species, each with the simple exponential form (as a function of altitude  $r$  above the lunar surface),  $n = n_0 e^{-r/H}$ , where each ion has its own scale height  $H$  and production rate (subsolar density  $n_0$  times ionization rate), for a total of 10 free parameters. This simple model does not explicitly include a sputtering source of ions from the surface (although we did experiment with such a parameterization), but if the fit indicates a very low scale height, it may implicate a contribution from sputtering.

#### 4. Best-Fit Models

[13] Figure 3 shows the result of a fit to masses 12, 16, 24, 28, and 40 (one should understand these as representing a range of masses near those values, with some of the candidate masses listed in Table 1), for the range of solar zenith angle constrained by our data. White contours outline the range of source points that constrain the fits for each mass as derived analytically from back-traced trajectories. This fit, with a normalized  $\chi^2$  value of 1.07, represents one of an ensemble of eight best fits taken from hundreds of runs with random initializations. (Because the inversion is non-linear, different initial assumptions lead to slightly different solutions; Table 1 shows the range of fit parameters for the entire ensemble.) For the fit in Figure 3, the five ion masses have scale heights of 48, 105, 220, 79, and 50 km and relative near-surface production rates of 1:2:0.98:3.7:5.4. Adjusting for the ionization rates, we infer near-surface densities of 2840, 11,300, 121, 10.5, and 19,600  $\text{cm}^{-3}$  (as

**Table 1.** Comparison of Our Source Model Fit Results with Previous Constraints [*Stern*, 1999] (S99) and Predictions From *Sarantos et al.* [2012a] (S2012)<sup>a</sup>

	Photo Rate (5/8/12)	S99 Subsolar Density (cm <sup>-3</sup> )	S2012 Subsolar Density (cm <sup>-3</sup> )	S2012 Column Depth (cm <sup>-2</sup> )	Density Upper Limit (cm <sup>-3</sup> )	Column Depth Upper Limit (cm <sup>-2</sup> )	Best-Fit Five-Species Model Density (cm <sup>-3</sup> )	Best-Fit Five-Species Model Column Depth (cm <sup>-2</sup> )	Best-Fit H (km)
<b>He</b>	$1.4 \times 10^{-7}$	2000			1600	$7.9 \times 10^{10}$			
<b>C</b>	$6.8 \times 10^{-7}$	<200			4400	$6.2 \times 10^{10}$	2100–3200	$1.1\text{--}1.2 \times 10^{10}$	31–58
<b>O</b>	$3.5 \times 10^{-7}$	<500	83.2	$8.1 \times 10^9$	12,000	$2.2 \times 10^{11}$	8500–11,400	$9\text{--}11.6 \times 10^{10}$	98–126
<b>CH<sub>4</sub></b>	$4.7 \times 10^{-7}$	10,000			8500	$1.6 \times 10^{11}$	6300–8400	$6.8\text{--}8.5 \times 10^{10}$	
<b>OH</b>	$2.4 \times 10^{-7}$	$<1 \times 10^6$			<b>17,000</b>	<b><math>3.1 \times 10^{11}</math></b>	12,200–16,400	$1.3\text{--}1.7 \times 10^{11}$	
<b>Na</b>	$1.6 \times 10^{-5}$	70	60	$1.9 \times 10^9$	640	$8.3 \times 10^9$	42–260	$1.8\text{--}2.9 \times 10^9$	97–424
<b>Mg</b>	$2.9 \times 10^{-7}$	<6000	7.8	$7.3 \times 10^8$	36,000	$4.6 \times 10^{11}$	2400–14,500	$1.0\text{--}1.6 \times 10^{11}$	
<b>Al</b>	$6.9 \times 10^{-4}$	<55	6.6	$4.1 \times 10^8$	<b>18</b>	<b><math>2 \times 10^8</math></b>	5.4–12.7	$6.7\text{--}10.7 \times 10^7$	71–173
<b>Si</b>	$2.4 \times 10^{-5}$	<48	23.3	$2.2 \times 10^9$	530	$5.8 \times 10^9$	160–370	$1.9\text{--}3.1 \times 10^9$	
<b>N<sub>2</sub></b>	$7.6 \times 10^{-7}$	800			16,000	$1.8 \times 10^{11}$	4900–11,500	$6.0\text{--}9.7 \times 10^{10}$	
<b>CO</b>	$5.9 \times 10^{-7}$	<14,000			21,000	$2.4 \times 10^{11}$	6300–15,000	$8.2\text{--}12 \times 10^{10}$	
<b>K</b>	$2 \times 10^{-5}$	17	19.1	$3.5 \times 10^8$	675	$4.2 \times 10^9$	400–520	$2.1\text{--}2.5 \times 10^9$	43–66
<b>Ca</b>	$7 \times 10^{-5}$	<1	6.1	$5.6 \times 10^8$	190	$1.2 \times 10^9$	110–150	$6.0\text{--}7.3 \times 10^8$	
<b>Ar</b>	$5.3 \times 10^{-7}$	100,000			<b>25,000</b>	<b><math>1.6 \times 10^{11}</math></b>	15,000–19,700	$7.9\text{--}9.6 \times 10^{10}$	
<b>CO<sub>2</sub></b>	$1.7 \times 10^{-6}$	1000			7800	$5.0 \times 10^{10}$	4700–6200	$2.5\text{--}3.0 \times 10^{10}$	
<b>Fe</b>	$1.7 \times 10^{-6}$	<380	8.6	$8.7 \times 10^8$	6400	$3.8 \times 10^{10}$			

<sup>a</sup>Best-fit columns list the range of parameters (column depth = subsolar density  $\times$  scale height  $H$  for each case) obtained from an ensemble of the best eight fits obtained from random initializations. Values for mass ranges with multiple species indicate abundances for each alternative alone; the real atmosphere could consist of an appropriately weighted combination of these sources, which produces the same total flux of photoions. To calculate source densities from production rates, we use cross-sections from Huebner and Mukherjee’s Photo Rate Coefficient Database [*Huebner et al.*, 1992] integrated over composite solar spectra from TIMED/SEE [*Woods et al.*, 2000] and SORCE SOLSTICE [*McClintock et al.*, 2005]. The derivation of the He limit required the assumption of a 500 km scale height to constrain the fit sufficiently. Values in bold indicate limits substantially lower than previous constraints.

displayed in Figure 3) if all the flux in each mass bin results solely from photoionization of C, O, Na, Al, and Ar, respectively. In fact, our fit only constrains total production rates, which result from a mix of various source processes (not limited to ionization of neutral exospheric constituents) and species contributing to that mass range. Table 1 shows the range of results for the entire ensemble of fits with similar  $\chi^2$  values, with alternative results assuming each possible species in each mass range.

[14] The normalized  $\chi^2$  value of 1.07 indicates a good fit, compared with a value of unity that would represent an essentially perfect fit, given errors (assuming we have not overestimated the latter). We have found slightly better fits (1.03–1.04) by allowing the exosphere to vary with solar zenith angle, but we achieve more consistent convergence with the angle-independent case. We have also considered models where each species has multiple scale heights, but we have not found better fits from such a model.

[15] Figure 4 shows the derived fluxes corresponding to the best-fit exosphere model of Figure 3, in the same format as Figure 2. Overall, we find a good match between observation and model. As discussed above, the  $\theta$  variation largely results from geometric constraints. However, the energy, time, and  $\varphi$  variation all provide significant information about the exospheric composition and structure. We note that our model slightly under-fits the peak of the observed fluxes. This could result from a poor choice of exospheric structure; however, we find similar results with every source model we have considered. Alternatively, it may result from trajectory reconstruction errors, which necessarily introduce errors in the independent as well as dependent variables of the fit and which no improvement in the source model can address.

[16] Figure 5 shows another set of plots in the same format as Figures 2 and 4, but colored according to the species, which contributes the largest amount of flux to each bin. We note that all five species in our fit contribute to the best-fit model fluxes. Quantitatively, our model predicts that masses 12, 16, 24, 28, and 40 contribute 6%, 25%, 20%, 27%, and 22% of the flux observed by ARTEMIS during this time period. Therefore, the observed fluxes do not result from a single dominant pickup ion species, an extremely important conclusion that may have significant implications for the analysis of other pickup ion observations.

[17] As indicated in Table 1, we find more consistent convergence for the model parameters for masses 12, 16, and 40 than for masses 24 and 28. Primarily, this results from significant colinearity between the nearby masses 24 and 28. Nonetheless, even for these masses, although subsolar production rate and scale height have larger variations, we find relatively consistent column depths. Our subsolar densities and column depths compare very favorably to known limits [*Stern*, 1999] and predictions [*Sarantos et al.*, 2012a] for masses 24, 28, and 40, assuming majority contributions from Na, Al, and Ar. At masses 12 and 16, though, we predict much higher neutral exospheric densities than expected from optical limits [*Feldman and Morrison*, 1991]. Wind observed significant fluxes of mass 16 pickup ions in the solar wind [*Mall et al.*, 1998]. Kaguya also found significant peaks consistent with masses 16 and 12 in both the solar wind and terrestrial magnetosphere [*Yokota et al.*, 2009; *Tanaka et al.*, 2009]. Mass 12 comprises only a small portion of the observed fluxes in our fit and does not contribute significantly to the angles and energies with the highest observed fluxes, so we should not place too much weight on

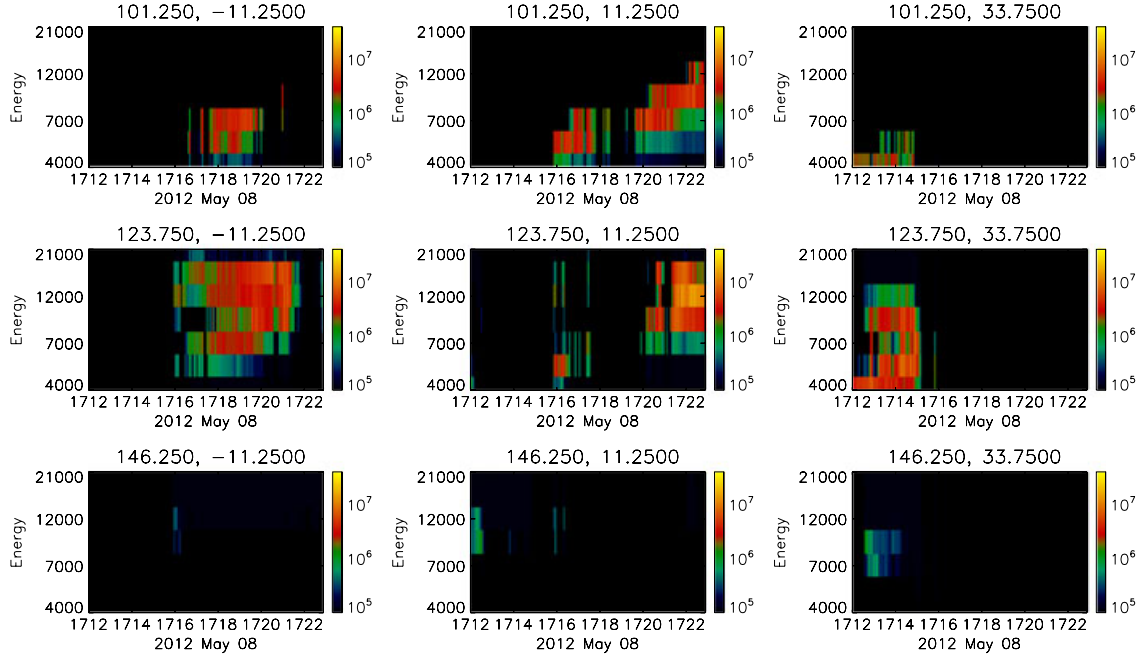


**Figure 4.** Best-fit pickup ion fluxes produced from the source model shown in Figure 3 and described in the text and Table 1, in the same format as Figure 2.

this result. Mass 16, however, comprises  $\sim 25\%$  of the flux in the best-fit cases, and a fit without mass 16 has a normalized  $\chi^2$  value of 1.19, significantly worse than the fit with it present.

[18] The large contribution to the best-fit model from mass 16 violates known optical limits for O [Feldman and Morrison, 1991] by a factor of  $\sim 20$ . However, several possible resolutions exist. First, terrestrial O may “seed” the lunar surface during its passage through the magnetosphere,

resulting in a transient O exosphere. Alternatively, OH or CH<sub>4</sub> (the former at mass 17), both allowed by known limits, may comprise a significant portion of the observed flux. The presence of significant quantities of either molecule in the lunar atmosphere would have significant implications as sinks of solar wind H, and C in the second case [Hodges, 1976].

[19] The best-fit scale heights also prove informative. For thermally accommodated species, we expect scale heights

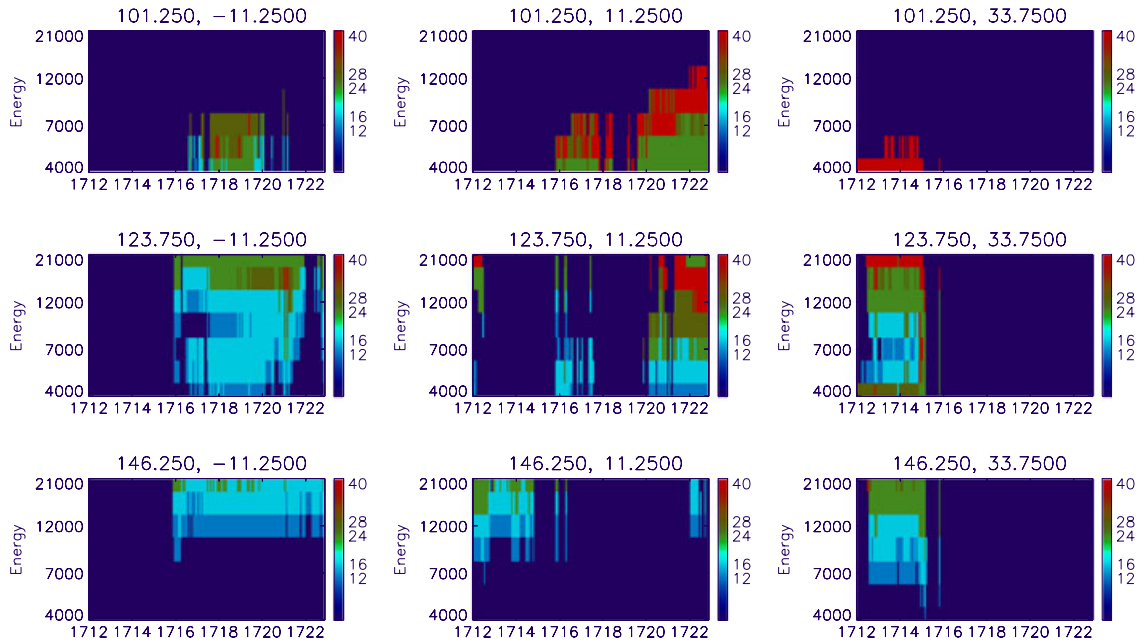


**Figure 5.** Major contributions to measured differential energy flux, colored by the dominant ion mass at each energy, angle, or time, for the best-fit source model shown in Figure 3, in the same format as Figures 2 and 4.

on the order of 160, 120, 80, 70, and 50 km for the five masses. For masses 16 and 40, we find scale heights very much consistent with thermal accommodation. We expect thermal accommodation for Ar at mass 40 but find it somewhat surprising for O at mass 16, which one might expect to have a significant sputtered component. This result may indicate a substantial cold O component or may again point to the alternatives of OH or CH<sub>4</sub>. For masses 24 and 28, we find somewhat higher scale heights, still roughly consistent with thermal release of neutrals from the surface, but allowing for some contribution from a more energetic release process such as sputtering or micrometeorite impacts (as expected for Na at mass 23 in particular). Finally, we predict a scale height too low for even a thermally accommodated species for mass 12, suggesting a significant contribution from direct production of ions from the surface (which could resolve the apparent violation of optical limits on exospheric densities for this mass range).

## 5. Neutral Exosphere Upper Limits

[20] As a final application of our model, we derive upper limits on the species that comprise the lunar atmosphere. We accomplish this very simply by applying the same methodology above but fitting the entire ARTEMIS observation to an exosphere consisting of a single mass range. By assuming that the resulting best-fit production rate derives entirely from photoionization of a single species, we obtain an upper limit on the abundance (because multiple species and ion production processes actually contribute). For He, because we had rather poor spatial coverage (not extending to the surface) for our constraints, we had to assume a scale height consistent with thermal accommodation to derive an upper limit. For all other species, the scale height remains a free parameter in the fit.

[21] For the most part, our limits (Table 1) prove less stringent than existing limits. However, we can place stronger limits (a factor of 3 and 60, respectively) on Al and OH neutral atmospheric abundances than previous observations. For OH, only a very weak limit previously existed. Al, on the other hand, has such a high photoionization yield that only a small amount can exist without Al dominating the pickup ion flux (not the case, according to our results and previous measurements). Our upper limit for Ar also lies significantly below that tabulated in *Stern* [1999]. We note that the Lunar Reconnaissance Orbiter Lyman Alpha Mapping Project has also not yet observed Ar [*Stern et al.*, 2012], suggesting the possibility of lower present-day Ar density than in the Apollo era.

[22] We note that we have only addressed upper limits on each species individually. By considering all species in each mass range simultaneously, we could provide stronger joint limits on groups of species. For instance, if one took the abundance of one species in a mass group as a given (based on existing or future data), one could derive a stronger upper limit on other species in that mass group. We leave such exercises for future work.

## 6. Implications

[23] This work demonstrates the feasibility of using pickup ion measurements from orbit, even in the absence

of detailed composition information, to place real constraints on the composition and structure of the lunar atmosphere. This particular observation had relatively unique characteristics, because the Moon was just completing its transit of the terrestrial magnetosphere. At this time, the Moon had resided in the flowing plasma of the magnetosheath for ~30 h, which may or may not have provided enough time to replenish the species in the neutral exosphere that have a contribution from solar wind species and/or solar wind sputtering from the surface, especially those such as helium that primarily derive from the solar wind [*Feldman et al.*, 2012]. In the future, it should prove instructive to compare similar measurements at various lunar phases to determine the efficacy of various processes in producing the tenuous lunar atmosphere and constrain the temporal and spatial variability of that atmosphere. To do so, we will need to obtain burst data at times when the spacecraft crosses the pickup ion plume. No doubt, this may again happen fortuitously; however, we also anticipate the possibility of developing special modes to trigger burst data collection at times and locations where we can most easily observe pickup ions from the near-lunar environment.

[24] **Acknowledgments.** We thank the NASA Lunar Science Institute for support and acknowledge NASA contract NASS-02099 for THEMIS/ARTEMIS support. We thank K.-H. Glassmeier and U. Auster for the use of FGM data provided under the lead of the Technical University of Braunschweig and with financial support through the German Ministry for Economy and Technology and the German Center for Aviation and Space under contract 50 OC 0302. We thank the Photo-Rate Data Coefficient Data Base [<http://phidrates.space.swri.edu>] and the Laboratory for Atmospheric and Space Physics Interactive Solar Irradiance Datacenter site [<http://lasp.colorado.edu/lisird/missiondatafiles.html>] for access to cross-sections and solar spectra used to calculate photoionization rates.

## References

- Angelopoulos, V. (2010), The ARTEMIS mission, *Space Sci Rev*, doi:10.1007/s11214-010-9687-2, 2010.
- Feldman, P. D., and D. Morrison (1991), The Apollo 17 ultraviolet spectrometer: Lunar atmosphere measurements revisited, *Geophys. Res. Lett.*, *18*, 2105–2109.
- Feldman, P. D., D. M. Hurley, K. D. Retherford, G. R. Gladstone, S. A. Stern, W. Pryor, J. W. Parker, D. E. Kaufman, M. W. Davis, and M. H. Versteeg (2012), Temporal variability of lunar exospheric helium during January 2012 from LRO/LAMP, *Icarus*, *221*, 854–858.
- Halekas, J. S., A. R. Poppe, G. T. Delory, M. Sarantos, W. M. Farrell, V. Angelopoulos, and J. P. McFadden (2012), Lunar pickup ions observed by ARTEMIS: Spatial and temporal distribution and constraints on species and source locations, *J. Geophys. Res.*, *117*, E06006, doi:10.1029/2012JE004107.
- Hartle, R. E., M. Sarantos, and E. C. Sittler Jr. (2011), Pickup ion distributions from three-dimensional neutral exospheres, *J. Geophys. Res.*, *116*, A10101, doi:10.1029/2011JA016859.
- Hodges, R. R., Jr. (1976), The escape of solar-wind carbon from the moon, *Proc. Lunar Sci. Conf.*, *7th*, 493–500.
- Hoffman, J. H., and R. R. Hodges, Jr. (1975), Molecular gas species in the lunar atmosphere, *The Moon*, *14*, 159–167.
- Hoffman, J. H., R. R. Hodges Jr., and D. E. Evans (1973), Lunar atmospheric composition results from Apollo 17, *Proc. Lunar Sci. Conf.*, *4*, 2875.
- Huebner, W. F., J. J. Keady, and S. P. Lyon (1992), Solar photo rates for planetary atmospheres and atmospheric pollutants, *Astrophys. Space Sci.*, *195*, 1–294.
- Lue, C., Y. Futaana, S. Barabash, M. Wieser, M. Holmstrom, A. Bhardwaj, M. B. Dhanya, and P. Wurz (2011), Strong influence of lunar crustal fields on the solar wind flow, *Geophys. Res. Lett.*, *38*, doi:10.1029/2010GL046215.
- Mall, U., E. Kirsch, K. Cierpka, B. Wilken, A. Soding, F. Neubauer, G. Gloeckler, and A. Galvin (1998), Direct observation of lunar pickup ions near the Moon, *Geophys. Res. Lett.*, *25*, 3799–3802.
- McClintock, W. E., G. J. Rottman, and T. N. Woods (2005), Solar Stellar Irradiance Comparison Experiment II (SOLSTICE II): Instrument concept and design, *Solar Physics*, *230*, 225–258.

- McFadden, J. P., C. W. Carlson, D. Larson, M. Ludlam, R. Abiad, B. Elliott, P. Turin, M. Marckwordt, and V. Angelopoulos (2008), The THEMIS ESA plasma instrument and in-flight calibration, *Space Sci. Rev.*, *141*, 277–302.
- Potter, A. E., and T. H. Morgan (1988), Discovery of sodium and potassium vapor in the atmosphere of the Moon, *Science*, *241*, 675–680.
- Saito, Y., et al. (2008), Solar wind proton reflection at the lunar surface: Low energy ion measurements by MAP-PACE onboard SELENE (KAGUYA), *Geophys. Res. Lett.*, *35*, L24205, doi:10.1029/2008GL036077.
- Sarantos, M., R. M. Killen, D. A. Glenar, M. Benna, T. J. Stubbs (2012a), Metallic species, oxygen and silicon in the lunar exosphere: Upper limits and prospects for LADEE measurements, *J. Geophys. Res.*, *117*, A03103, doi:10.1029/2011JA010744.
- Sarantos, M., R. E. Hartle, R. M. Killen, Y. Saito, J. A. Slavin, A. Gloer (2012b), Flux estimates of ions from the lunar exosphere, *Geophys. Res. Lett.*, doi:10.1029/2012GL052001.
- Stern, S. A. (1999), The lunar atmosphere: History, status, current problems, and context., *Rev. Geophys.*, *37*, 453–491.
- Stern, S. A., K. D. Retherford, C. C. C. Tsang, P. D. Feldman, W. Pryor, G. R. Gladstone (2012), Lunar atmospheric helium detections by the LAMP UV spectrograph on the Lunar Reconnaissance Orbiter, *Geophys. Res. Lett.*, *39*, L12202, doi:10.1029/2012GL051797.
- Tanaka, T., et al. (2009), First in situ observation of the Moon-originating ions in the Earth's magnetosphere by MAP-PACE on SELENE (KAGUYA), *Geophys. Res. Lett.*, *36*, L22106, doi:10.1029/2009GL040682.
- Woods, T. N., S. M. Bailey, F. G. Eparvier, G. M. Lawrence, J. Lean, W. E. McClintock, R. G. Roble, G. J. Rottman, S. C. Solomon, W. K. Tobiska, and O. R. White (2000), The TIMED solar EUV experiment, *Physics and Chemistry of the Earth, Part C: Solar, Terrestrial & Planetary Science*, *25*, 5-6, 393–396, doi:10.1016/S1464-1917(00)00040-4.
- Yokota, S., et al. (2009), First direct detection of ions originating from the Moon by MAP-PACE IMA onboard SELENE (KAGUYA), *Geophys. Res. Lett.*, *36*, L11201, doi:10.1029/2009GL038185.